Joint PAZ & TanDEM-X Mission Interferometric Experiments: Interoperability and Products

Alberto Alonso-González ⬤, *Member, IEEE*, Nuria Gimeno Martínez, Irena Hajnsek, *Fellow, IEEE*,
Patricia Cifuentes Revenga, María José González Bonilla, Christo Grigorov, Achim Roth, Ursula Marschalk,
Nuria Casal Vázquez, Juan Manuel Cuerda, and Marcos García Rodríguez

Abstract—This article analyzes the potential synergies between the two German satellites of the TerraSAR-X/TanDEM-X (TSX/TDX) mission and the Spanish PAZ satellite. Since both platforms are almost identical and they were launched in the same orbital plane, comparable images of the same area under the same geometry may be regularly acquired by both systems. This allows the simultaneous exploitation of both missions for building larger time series and improving the revisit time of 11 days for each mission up to 4 or 7 days while combining both. The geometric accuracy and the interferometric performance when combining both sensors are investigated, considering different acquisition parameters and land cover types. For this article several images are acquired over German and Spanish calibration test sites. The results obtained when combining acquisitions from satellites of the TSX/TDX and PAZ missions show no loss of performance with respect to image pairs of the same satellite, indicating that both missions might be exploited synergistically in order to improve current monitoring applications or maybe to allow newer application with tighter requirements in terms of revisit time or temporal coverage. In order to explore all these possibilities, a call for scientific proposals will be jointly opened by the coordinators of the scientific activities of both missions in order to explore the simultaneous exploitation of TSX/TDX and PAZ data.

Index Terms—Bistatic synthetic aperture radar (SAR), constellation, digital elevation model (DEM), PAZ, SAR interferometry, TerraSAR/TanDEM-X (TSX/TDX).

I. INTRODUCTION

THE main objective of this article is to analyze the interoperability between sensors from a scheduled experiment between TerraSAR-X/TanDEM-X (TSX/TDX) [1], [2] and PAZ

Alberto Alonso-González and Christo Grigorov are with the Microwaves and Radar Institute, German Aerospace Center, 82234 Wessling, Germany (e-mail: alberto.alons@gmail.com; christo.grigorov@dlr.de).

Nuria Gimeno Martínez, Patricia Cifuentes Revenga, María José González Bonilla, Nuria Casal Vázquez, Juan Manuel Cuerda, and Marcos García Rodríguez are with the Instituto Nacional de Técnica Aeroespacial, 28850 Madrid, Spain (e-mail: gimenon@inta.es; pcifuentes@isdefe.es; glezbmj@inta.es; casalv@inta.es; cuerdamjm@inta.es; garciarm@inta.es).

Irena Hajnsek is with the Microwaves and Radar Institute, German Aerospace Center, 82234 Wessling, Germany, and also with the Institute of Environmental Engineering, ETH Zurich, 8093 Zurich, Switzerland (e-mail: irena.hajnsek@dlr.de).

Achim Roth and Ursula Marschalk are with the German Remote Sensing Data Center, German Aerospace Center, 82234 Wessling, Germany (e-mail: achim.roth@dlr.de; ursula.marschalk@dlr.de).

Digital Object Identifier 10.1109/JSTARS.2021.3084401

satellites. Both missions operate successfully with respect to their respective user and national radar program requirements. TSX/TDX as well as PAZ [24], [25] are closely identical systems and are delivering data products in a 11-day repeat pass orbit. However, when both systems are operated in a constellation, then repeat times of four days and seven days can be realized as well. The advantage of using shorter repeat times is especially important for monitoring highly dynamic processes [30] and is therefore relevant for all applications where fast changes are of importance to be captured (e.g., monitoring agricultural phenological changes, changes due to snow cover, any kind of deformation studies and many more). One of the most important observables is the interferometric coherence that is indeed essential for retrieving very accurate height information. Depending on the repeat time in relation to the changes occurring on the surface the interferometric coherence shows a fast decay and is decorrelating such that no reliable information can be retrieved from the interferometric coherence as well as the interferometric phase. This is already the case in an 11-day repeat time for a radar system with higher transmit frequency as *X*-band. The opportunity to coherently combine three satellites from two different missions is unique and is promising for some applications to be of relevance to obtain and keep the accuracy of the observables stable, when shortening the repeat times. The main objective of this study is to assess the performance of the interferometric coherence and phase when combining TSX/TDX and PAZ acquisitions in terms of stability and accuracy. For this an own experiment was conducted over two main calibration sites, where calibration devices have been used to quantify the performance of the observables, the location and radiometric accuracy. The reasoning for such an assessment is to provide access to the data and open it for the science community. In the following sections the experiment, the data and the assessment are presented.

II. MISSION DESCRIPTION

TanDEM-X is an extension of the TerraSAR-X radar mission [2], [3], co-flying a second satellite of nearly identical capability in a close formation. The TerraSAR-X satellite (TSX), as the basis for TanDEM-X, was successfully launched into a sun-synchronous dusk-dawn orbit with 97.44° inclination on June 15, 2007. The nominal orbit height is 514.8 km and the orbit repeat cycle is 11 days. TSX has already built in

all necessary features required for the implementation of the TanDEM-X mission. Examples are additional *X*-band horn antennas for inter-satellite phase synchronization, the availability of a dual-frequency GPS receiver for precise orbit determination, excellent RF phase stability of the SAR instrument, and PRF synchronization based on GPS as a common time reference. The second satellite, TDX, launched June 21, 2010, is a rebuild of TSX with only minor modifications like an additional cold gas propulsion system for formation fine tuning, double-sized on-board solid-state memory for increased data recording capacity, and an additional *S*-band receiver to enable the reception of telemetry and GPS position information broadcast by TSX. The instruments on both satellites are advanced high-resolution *X*-band (center frequency 9.65 GHz, chirp bandwidth up to 300 MHz) synthetic aperture radars (SAR), which can be operated in Spotlight, Stripmap, and ScanSAR mode with full polarization capability [4]. The active phased array antenna enables agile beam pointing and flexible beam shaping as required for the acquisition of a wide range of image products with varying resolutions and scene sizes. TanDEM-X can acquire interferometric data in different configurations [1], such as bistatic, monostatic, and alternating bistatic modes. The different interferometric configurations can be further combined with different TSX and TDX SAR imaging modes, such as Stripmap, ScanSAR, and Sliding Spotlight. Operational DEM generation is performed using the bistatic Stripmap mode in single polarization.

PAZ mission is the SAR component of the Spanish National Program for Earth Observation by Satellite. PAZ was launched on February 22, 2018 from California, being the mission declared operational in early September. The space segment of PAZ mission is owned by Hisdesat Servicios Estratégicos S.A., the mission operator, whereas the Spanish National Institute of Space Technology (INTA) is in charge of Ground Segment development and mission Science Activities. PAZ platform is a heritage of TSX/TDX, with a newly developed front-end by Astrium-Spain. With the goal of achieving a constellation composed of three almost identical satellites, PAZ was launched in the same orbital plane as TerraSAR-X and TanDEM-X, orbiting ahead of TerraSAR-X, with an offset of 98.18° in true anomaly. Furthermore, in order to accomplish constellation needs, PAZ operational modes have been established following the definition made by DLR for TerraSAR-X and TanDEM-X [26].

III. Experiments Description

The interferometric experiments between PAZ and TSX/TDX sensors have been conducted over three different test sites in Neustrelitz, northern Germany, and in Madrid and Albacete, Spain. Fig. 1 shows the location of the corner reflectors (CR) available on these test sites.

A. Imaging Mode for PAZ and TDX

For the experiments conducted on this paper, the Stripmap imaging mode in single polarization was employed for PAZ and TSX/TDX sensors with a chirp bandwidth of 100 or 150 MHz. The ground resolution is 3.3 m in azimuth and from 2.9 to 2.5 m in range, depending on the incidence angle. For each

Fig. 1.　INTA—DLR interferometric experiments test sites.

test site some acquisitions have been acquired in HH and in VV polarizations in both sensors. The following section will describe in more detail the acquisitions performed on each test site and the corresponding acquisition parameters.

The following subsections provide a more detailed description of the selected test sites. Furthermore, Tables I to V list for each test site the information of all data acquisitions for both missions and their perpendicular baseline with respect to the master image, marked in bold. On these tables TSX, TDX, and PAZ refer to monostatic images taken by each one of the satellites of the TanDEM-X and the PAZ missions. Single-pass bi-static images acquired simultaneously by both German satellites flying in close formation appear as TSX-TDX.

B. Neustrelitz

The calibration site that is used for the long-term monitoring of the TSX and TDX instrument radiometric stability is located near Neustrelitz in northern Germany. It is deployed within the DLR satellite ground station premises there and consists of three CR of 1.5 m length. Regular acquisitions have been planned and executed by both satellites since their respective launch in 2007 and 2010 and their evaluation shows no degradation of the SAR instruments to this day [6], [7]. The CRs are permanently aligned in accordance with two different SAR geometries: strip 11 and strip 6 [8]. The surrounding area is mainly flat and covered with forest and agricultural areas. Additionally, some lakes may be observed on the images.

Table I and II give both monostatic and bistatic acquisitions performed over this test site by TSX, TDX, and PAZ, which have been evaluated here, and their perpendicular baseline with respect to the master image, marked in bold. Each table shows the acquisitions performed on different geometry: strip 11 and strip 6, as PAZ beams are equivalent to TDX and TSX [8], [32], which briefly correspond to incidence angles of around 39° and 29°, respectively.

As an example, Fig. 2 shows two amplitude images of the Neustrelitz strip 11 dataset at VV polarization.

TABLE I
ACQUISITIONS NEUSTRELITZ STRIP 11

Satellite	Acq. Time	Pol.	Perp. Baseline [m]
PAZ	2019.12.07	VV	-163
TSX	**2019.12.14**	**VV**	**-**
PAZ	2019.12.18	VV	-6
PAZ	2020.01.20	VV	-141
TSX	2019.11.22	HH	-67
PAZ	2019.11.26	HH	33
TSX	2019.12.25	HH	60
PAZ	2019.12.29	HH	130
PAZ	2020.01.09	HH	25
TSX	**2020.01.27**	**HH**	**-**
PAZ	2020.01.31	HH	1
TSX-TDX	2020.01.16	VV	108

TABLE II
ACQUISITIONS NEUSTRELITZ STRIP 6

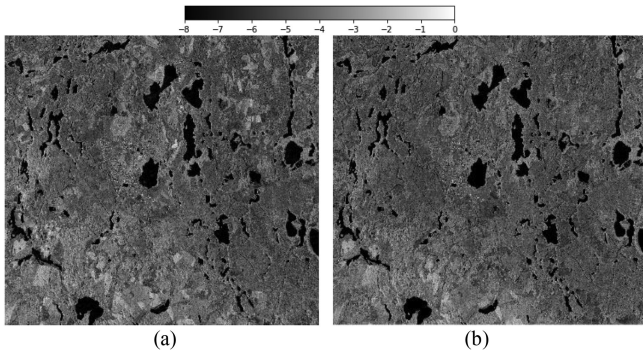| Satellite	Acq. Time	Pol.	Perp. Baseline [m]
PAZ	2019.12.07	VV	10
TDX	**2019.12.12**	**VV**	**-**
PAZ	2019.12.18	VV	-127
PAZ	2020.01.20	VV	-16
PAZ	2019.11.24	HH	116
PAZ	2019.12.27	HH	47
TDX	**2020.01.03**	**HH**	**-**
PAZ	2020.01.07	HH	179
PAZ	2020.01.29	HH	-119
TDX	2020.02.05	HH	-30
TDX	2020.03.09	HH	31
TSX-TDX	2020.01.25	VV	39

Fig. 2. Amplitude images (in dB) for two VV images of Neustrelitz strip 11 dataset. (a) PAZ acquisition on 2019.12.07. (b) TDX on 2019.12.14.

TABLE III
ACQUISITIONS MADRID STRIP 4

Satellite	Acq. Time	Pol.	Perp. Baseline [m]
TDX	2019.12.05	VV	97
TDX	**2020.01.08**	**VV**	**-**
PAZ	2020.01.22	VV	292
TDX	2019.11.24	HH	11
PAZ	2019.11.28	HH	448
PAZ	2019.12.09	HH	340
TDX	**2019.12.16**	**HH**	**-**
PAZ	2020.01.11	HH	468
TSX-TDX	2019.12.27	VV	116
TSX-TDX	2020.01.07	HH	109

TABLE IV
ACQUISITIONS MADRID STRIP 13

Satellite	Acq. Time	Pol.	Perp. Baseline [m]
TSX	**2019.12.11**	**VV**	**-**
PAZ	2019.12.26	VV	51
PAZ	2020.01.17	VV	-74
PAZ	2019.11.23	HH	-85
PAZ	2019.12.04	HH	-2
TSX	2019.12.22	HH	50
PAZ	2020.01.06	HH	8
TSX	**2020.01.24**	**HH**	**-**
PAZ	2020.01.28	HH	176
TDX	2020.02.04	HH	-115
TDX	2020.02.15	HH	-296
TSX	2020.03.08	HH	-59
TSX	2020.03.19	HH	-71
TSX-TDX	2020.01.02	VV	119
TSX-TDX	2020.01.13	HH	115

TABLE V
ACQUISITIONS ALBACETE STRIP 13

Satellite	Acq. Time	Pol.	Perp. Baseline [m]
TDX	2019.12.06	VV	58
PAZ	2019.12.21	VV	282
PAZ	2020.01.01	VV	422
TDX	**2020.01.19**	**VV**	**-**
PAZ	2020.01.23	VV	338
TDX	**2019.11.25**	**HH**	**-**
PAZ	2019.11.29	HH	379
PAZ	2019.12.10	HH	337
TSX	2019.12.17	HH	183
PAZ	2020.01.12	HH	405
TSX-TDX	2019.12.28	VV	123
TSX-TDX	2020.01.08	HH	117

C. Madrid and Albacete

The Spanish test sites for these experiments, Madrid and Albacete, have been selected from two of the calibration fields designed by INTA for PAZ Commissioning Phase and nominal calibration activities [27]. In these test sites two sizes of Corners Reflectors are deployed, 1 and 1.5 m having their geographic coordinates accurately determined in WGS84, ITRF 2014 epoch 2010.

Madrid area comprises a total of ten CRs in two different regions surrounding Madrid City. Albacete calibration field comprises a total of seven CRs, all of them in agricultural flat areas. Tables III to V give the acquisitions performed over Madrid and Albacete on different geometry: strip 4 and strip 13, which briefly correspond to an incidence angle of around 24°

and 43°, respectively. Fig. 3 shows two amplitude images over the Albacete test site at HH polarization acquired by TDX and PAZ satellites.

IV. EXPERIMENTS ANALYSIS

A. Interferometric Phase and Coherence Stability

For the assessment of the interoperability of both constellations for interferometric processing, the interferometric phase and coherence will be analyzed in this section [5], [21]. The main goals of this article are as follows.

1) Compare the interferometric phase and coherence obtained between PAZ and TanDEM-X acquisition pairs with those obtained when using image pairs of the same sensor.
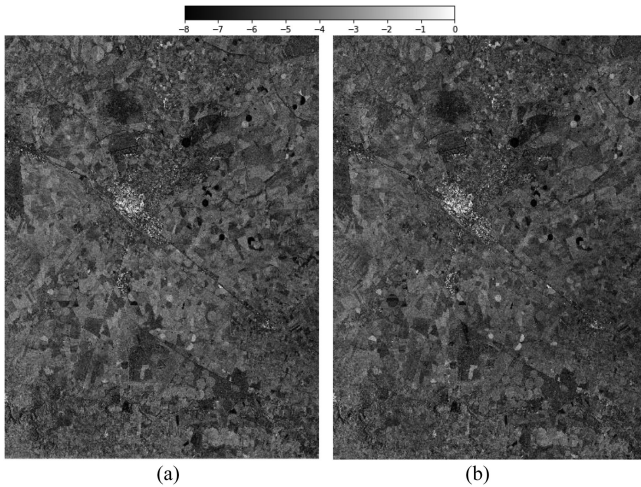
Fig. 3. Amplitude images (in dB) for two HH images of Albacete strip 13 dataset. (a) TDX acquisition on 2019.11.25. (b) PAZ on 2019.11.29.
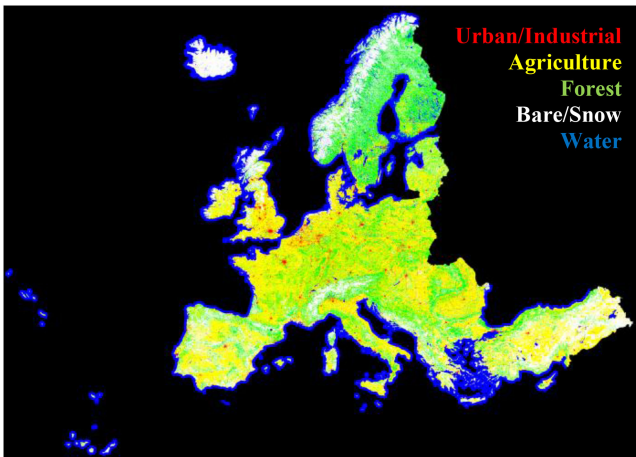

Fig. 4. CLC map from 2018, reduced to the five land cover classes described: urban and industrial in red, agricultural areas in yellow, forest in green, pastures, bare, and snow areas in white and water in blue colors.
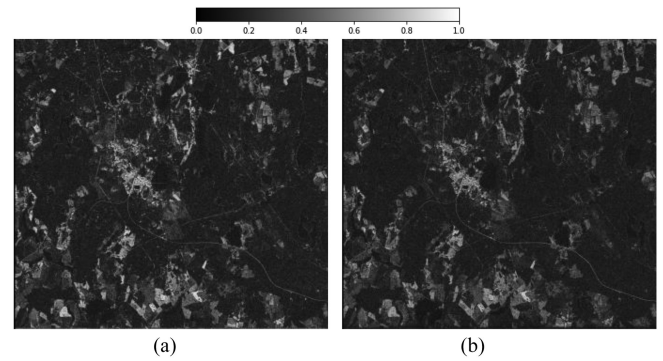

Fig. 5. Coherence obtained between two TSX acquisitions and one TSX-PAZ pair of the Neustrelitz strip 11 dataset at HH polarization with (a) 33 and (b) 29 days temporal separation and (a) 60 and (b) 130 m perpendicular baseline. Coherence mean ($\pm$ standard deviation σ) values. (a) 0.32 ($\pm$0.17). (b) 0.31 ($\pm$0.16). (a) Coherence TSX 2019.12.25 and TSX 2020.01.27. (b) Coherence PAZ 2019.12.29 and TSX 2020.01.27.
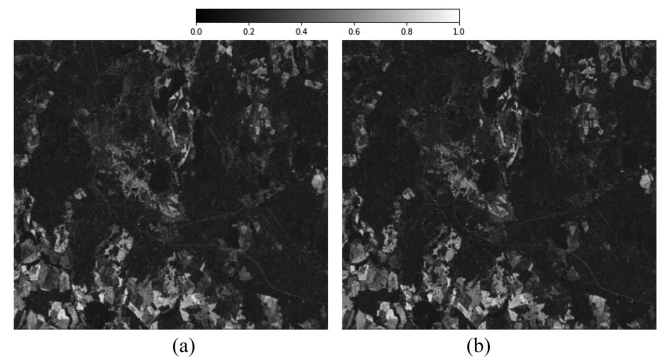

Fig. 6. Coherence obtained between TSX and PAZ Neustrelitz strip 11 acquisitions at VV polarization with (a) 7 and (b) 4 days temporal separation and (a) -163 and (b) -6 m perpendicular baseline. Coherence mean ($\pm\sigma$) values. (a) 0.32 ($\pm$0.18). (b) 0.32 ($\pm$0.18). (a) Coherence PAZ 2019.12.07 and TSX 2019.12.14. (b) Coherence TSX 2019.12.14 and PAZ 2019.12.18.

2) Discuss the practical limitations imposed by the sensors parameters in terms of the coherence obtained on the different land cover types.

For the discussion of the applicability to different land cover types, the ESA Corine land cover (CLC) of 2018 [9] will be used. This dataset has 100 m resolution and covers the whole of Europe. Therefore, all the previously presented test sites are covered and represented homogeneously by the same land cover classes. However, since the CLC has many different land-cover classes (44 in total), here they have been reduced to five main classes.

1) Urban and industrial areas, represented in red color.
2) Agricultural areas, represented in yellow.
3) Forested areas, in green color.
4) Pastures, bare and snow areas, appearing in white color.
5) Water covered areas, in blue color.

The plot of the previously described simplified CLC 2018 map is shown in Fig. 4.

In order to compare the coherence obtained between two TSX acquisitions with one pair of TSX and PAZ images, Fig. 5 shows the comparison between two pairs with a similar temporal separation around 1 month (33 and 29 days, respectively). It may be clearly seen that both pairs present very similar coherence values over the whole image, which suggest a good interoperability between both sensors. The coherence values, however, are considerably low in this test site. The areas presenting lower coherence correspond to forested areas. Although the perpendicular baseline between these pairs is different (60 and 130 m, respectively), no significant difference in coherence is observed. This suggests that the main source of coherence decorrelation in these areas is temporal decorrelation [10], [11], as it seems to be independent of the baseline.

To see more clearly the effect of changing the temporal and perpendicular baselines, Fig. 6 shows the coherence between two TSX-PAZ pairs with the shortest possible temporal separation, given by the sensors orbit: seven and four days, respectively. Interestingly, the image with four days separation also corresponds to almost zero-baseline geometry with a perpendicular baseline of just 6 m.
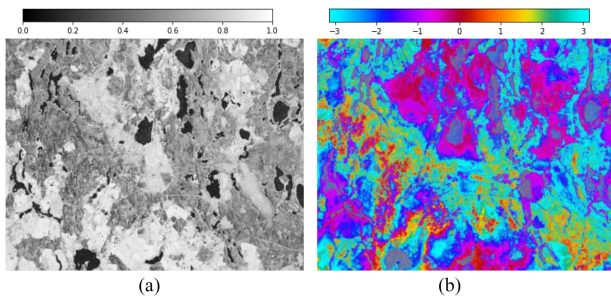
Fig. 7. (a) Coherence and (b) interferometric phase obtained for a single-pass bistatic TanDEM-X Neustrelitz strip 11 acquisition at VV polarization with 108 m perpendicular baseline. Coherence mean ($\pm \sigma$) values: 0.64 (± 0.22). (a) Coherence TSX-TDX 2020.01.16. (b) Int. phase TSX-TDX 2020.01.16.
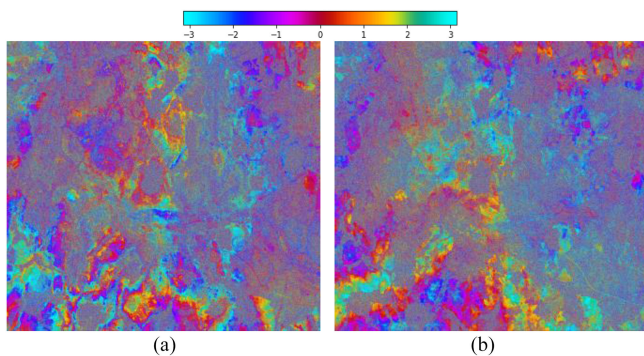

Fig. 8. Interferometric phase obtained between TSX and PAZ acquisitions at VV polarization with (a) 7 and (b) 4 days temporal separation and (a) -163 and (b) -6 m perpendicular baseline. (a) Int. phase PAZ 2019.12.07 and TSX 2019.12.14. (b) Int. phase TSX 2019.12.14 and PAZ 2019.12.18.

Comparing Fig. 6 with Fig. 5 it may be seen a small increase in the coherence of the agricultural fields, especially on the lower part of the image, but the coherence on the forested areas of the image still remains very low. Moreover, the fact that even at zero-baseline geometry the coherence goes close to 0, as in Fig. 6(b), confirms that volume decorrelation is not the responsible of this low coherence [13].

The single-pass bi-static acquisitions acquired by the TanDEM-X constellation may be employed in order to cancel the effect of temporal decorrelation, as master and slave acquisitions are acquired simultaneously [15]. Fig. 7 shows the coherence and phase obtained by the bi-static image acquired on January 16, 2020. Fig. 7(a) clearly presents a larger coherence over all the areas but it may also be observed a slightly lower coherence over forested areas. In this case, we can see the effect of volume decorrelation over forest, appearing in grey on the image [18]. For comparison purposes, Fig. 8 depicts the interferometric phase for the same pairs shown in Fig. 6. The comparison of Fig. 8(a) with Fig. 7(b) shows similar trends in the lower part of the image, related to the topography, but the low coherence over forested areas results in a noisy phase over most of the image.

As a consequence of this first analysis over Neustrelitz, it may not be clear if TanDEM-X and PAZ sensors are interoperable for interferometric acquisitions. The performance observed between TSX/TDX and PAZ pairs is equivalent to the performance when using only acquisitions of the same sensor. However, it has
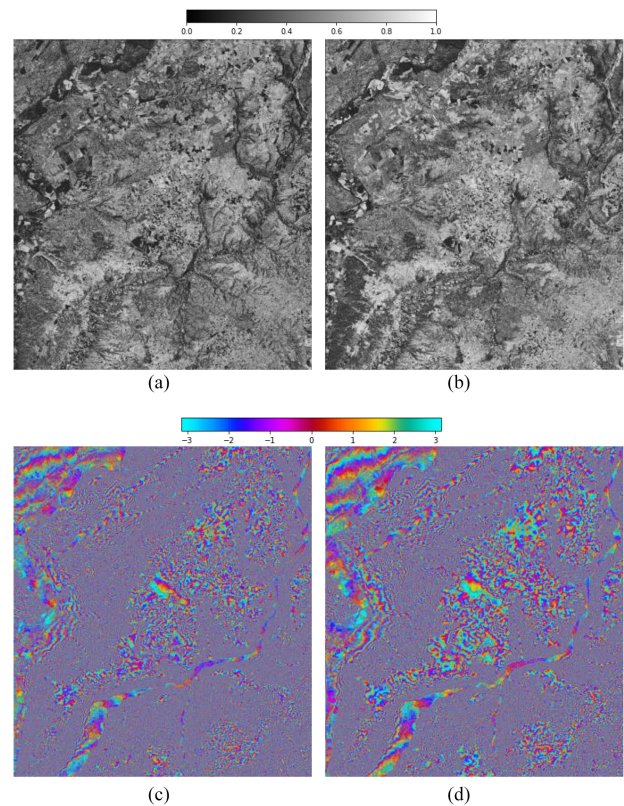

Fig. 9. Coherence (top row) and interferometric phase (bottom row) obtained between PAZ and TDX Madrid strip 4 acquisitions at HH polarization with (a) and (c) 18 and (b) and (d) 7 days temporal separation and (a) and (c) 448 and (b) and (d) 340 m perpendicular baseline. Coherence mean ($\pm \sigma$) values. (a) 0.51 (± 0.21). (b) 0.52 (± 0.22). (a) Coherence PAZ 2019.11.28 and TDX 2019.12.16. (b) Coherence PAZ 2019.12.09 and TDX 2019.12.16. (c) Int. phase PAZ 2019.11.28 and TDX 2019.12.16. (d) Int. phase PAZ 2019.12.09 and TDX 2019.12.16

also been observed that temporal decorrelation over forested areas at X-band is the main limitation for interferometric processing of repeat pass acquisitions. It may be seen that even with four days of temporal separation between acquisitions, enough temporal decorrelation is observed in order to lose completely the coherence over forest. Therefore, it is difficult to assess the interoperability with these results.

The data acquired over Madrid may be employed in order to analyze the behavior over a completely different land cover type. In this case, the strip 4 will be used as the scene covers an area with significant topography and less forested zones. Fig. 9 shows the coherence and interferometric phase between two different PAZ-TDX pairs with a temporal baseline of 18 and 7 days. In this case the spatial baseline is larger, 448 and 340 m, respectively. As it may be seen, the results obtained on this test site contrast strongly with those obtained over Neustrelitz. The coherence observed in Fig. 9(a) and (b) is generally higher over the whole scene. As a consequence, the obtained interferometric phase, in Fig. 9(c) and (d), is much less noisy, showing the underlying topography.

As a reference, Fig. 10 shows the interferometric coherence and phase for the single-pass bistatic image of the Madrid strip 4 dataset acquired at HH polarization by TanDEM-X. Note that
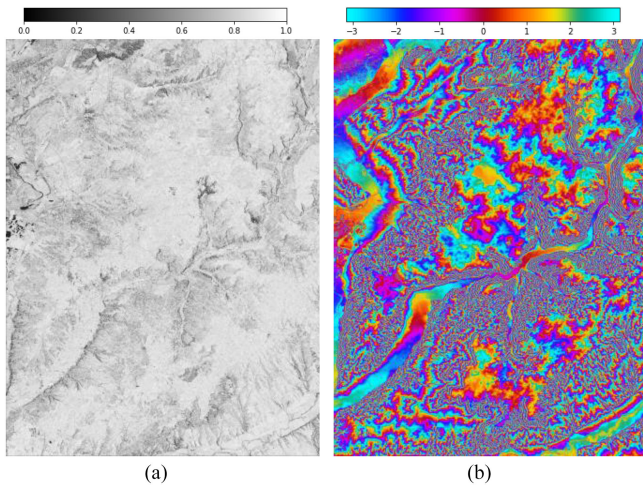
Fig. 10. (a) Coherence and (b) interferometric phase obtained for a single-pass bi-static TanDEM-X Madrid strip 4 acquisition at HH polarization with 109 m perpendicular baseline. Coherence mean ($\pm \sigma$) values: 0.81 ($\pm$0.13). (a) Coherence TSX-TDX 2020.01.07. (b) Int. phase TSX-TDX 2020.01.07
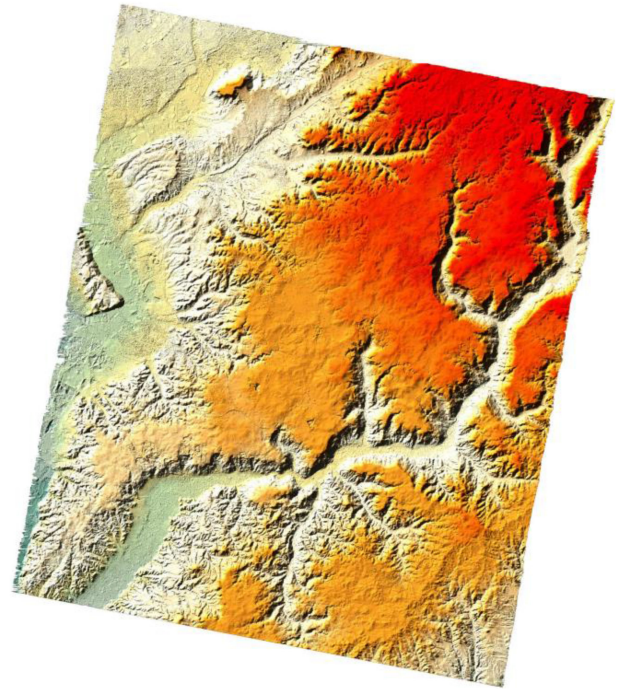

Fig. 11. 3-D representation (top view) of the geocoded DEM of Madrid generated from the interferogram between PAZ and TDX acquisitions of 2019.12.09 and 2019.12.16, respectively.

the scene coverage is not exactly the same and the bistatic image has a larger extent on the bottom part of the image. It may be seen, as expected, that the coherence is larger in Fig. 10, but the phase shown on the interferograms in Fig. 9 seems to closely represent the same topography features observed in Fig. 10. In this case, the repeat-pass presents a larger number of fringes than the single-pass interferograms due to the larger perpendicular baseline (448 and 340 m versus 109 m).

With the interferogram shown in the second column of Fig. 9(a) digital elevation model (DEM) has been obtained and is shown in Fig. 11. In this case a three-dimensional (3-D) representation of the obtained DEM, viewed from top, is presented in order to visualize more clearly the height changes. To our knowledge, this is the first demonstration of a DEM generated from a combination of two acquisitions of the different sensors of the TanDEM-X and PAZ missions.

The DEM obtained in Fig. 11 shows qualitatively most of the details of the scene topography at small scales. This is caused by the fact that a good coherence is obtained generally over the scene, with a mean value of 0.52. There are, however, some small areas where the coherence may be lost due to temporal decorrelation. Fig. 12(b) shows a zoom over a small area of the DEM in Fig. 11, corresponding to the upper left part of the image. Fig. 12(a) shows a zoom over the same area of the DEM obtained from the TanDEM-X bi-static acquisition shown in Fig. 10 [17]. Both DEMs accurately represent the same topographic details, but the DEM in Fig. 12(b) presents a block appearance on some slopes and some flat areas, especially in the lower left part, due to small areas with lower coherence. Despite these small details, the general quality of the repeat-pass DEM obtained with the PAZ and TDX interferogram seems considerably good.

To analyze more in detail the differences, Fig. 13(a) shows the difference between the single-pass TanDEM-X DEM, corresponding to the interferogram shown in Fig. 10, and the repeat-pass PAZ-TDX DEM shown in Fig. 11. The previously mentioned small differences may be seen, especially over areas

with significant slope. It may be seen also that there are some phase unwrapping areas concentrated over the borders of the image, where the coherence is generally lower. Despite these differences, however, most of the areas present a small error, as it may be seen in the error probability density function (PDF) shown in Fig. 13(b), where most of the values are concentrated around 0 m. The standard deviation of the error between the DEMs in this case is 8.36 m.

The Albacete test site presents a completely different land cover type. It is a flat area mainly covered by agricultural areas. This allows the analysis of the capabilities of interferometric acquisitions between PAZ and TanDEM-X for monitoring agricultural areas. Fig. 14 shows the interferometric coherence and phase between two TDX and PAZ acquisitions with four days of separation and a perpendicular baseline of 379 m. As it may be seen the coherence obtained over agricultural areas is generally high, resulting in a good quality interferometric phase in Fig. 14(b). It is worth noticing, however, that over the agricultural fields some appear with high coherence in bright color while a few others appear quite dark, losing most of the coherence. This binary effect has to do probably with the fact that some fields present a significant change in their radar response between these dates, losing their coherence due to temporal decorrelation. In Fig. 14, there is only a four days difference between the acquisitions and few fields present a change but, as long as the temporal separation between acquisitions increases, the number of fields appearing in black might increase significantly. This effect will be studied in more detail in Section IV-B.

In this case, due to the good coherence of the interferogram shown in Fig. 14, a DEM may be also generated for the Albacete
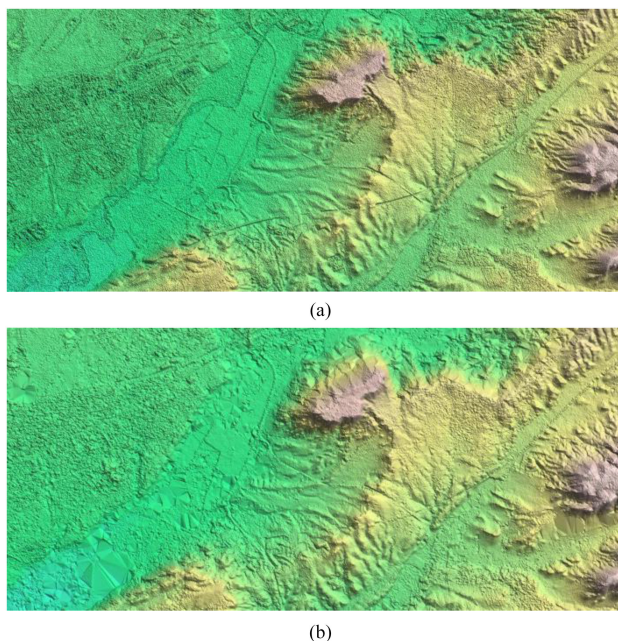
(a)

(b)

Fig. 12. Detail of the DEM obtained over Madrid with (a) the single-pass bi-static TanDEM-X interferogram shown at Fig. 9, and (b) the PAZ and TDX interferogram shown in Figs. 8(b) and 6(d). (a) DEM generated from a single pass TanDEM-X interferogram. (b) DEM generated from a repeat-pass PAZ and TDX interferogram.

(a)

(b)

Fig. 13. Height difference between the singe-pass and repeat-pass DEMs generated from the pairs shown in Figs. 10 and 9b and (d) and difference PDF. (a) Repeat-pass versus single-pass DEM difference. (b) Repeat-pass versus single-pass DEM difference histogram.

test site, which is shown in Fig. 15. Some topography may be observed on the top and bottom right parts of the image. As observed in the Madrid dataset, some block effects may be observed especially over some fields, which correspond to those fields where a change is observed, presenting lower coherences and appearing in black on Fig. 14(a).

The difference between the DEM shown in Fig. 15 and the corresponding single-pass bistatic DEM over Albacete is shown in Fig.16. In this case, the bistatic acquisition has a slightly different coverage and only covers an area corresponding to a bit more than the upper half of the TDX and PAZ acquisitions shown in Fig. 14. The errors shown in Fig. 16 show a different nature than those over the Madrid dataset, as shown in Fig. 13. In this case no phase unwrapping errors may be seen, characterized by a sudden change on the height difference, but a gradual deviation around range direction may be seen. In this case the standard deviation of the error increases to 16.26 m.

It is worth mentioning that since repeat-pass master and slave acquisitions are acquired at different atmospheric conditions, a differential atmospheric phase component may be added, which may add an additional error factor as this phase component is converted to height when generating repeat-pass DEMs [29]. Although there was not a significant impact in the repeat-pass DEM in Fig. 11, as shown in Fig. 13, a higher impact may be observed depending on the atmospheric conditions. This component, however, is generally more important at larger than smaller scales. This may be the effect generating the trend shown in Fig. 16. The atmospheric phase error will not be analyzed in detail here, as it is a common factor on any repeat-pass acquisition, independently of the sensor employed. Therefore, the
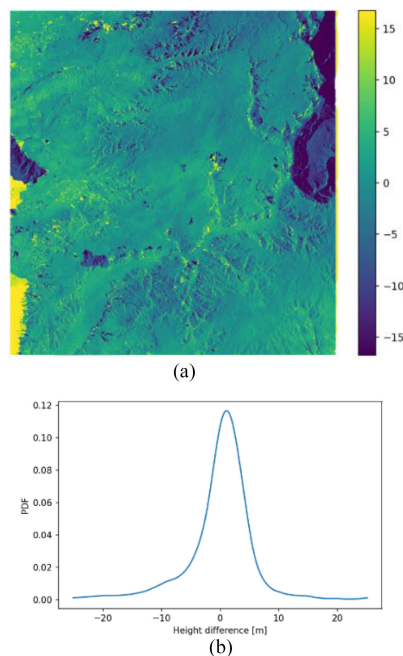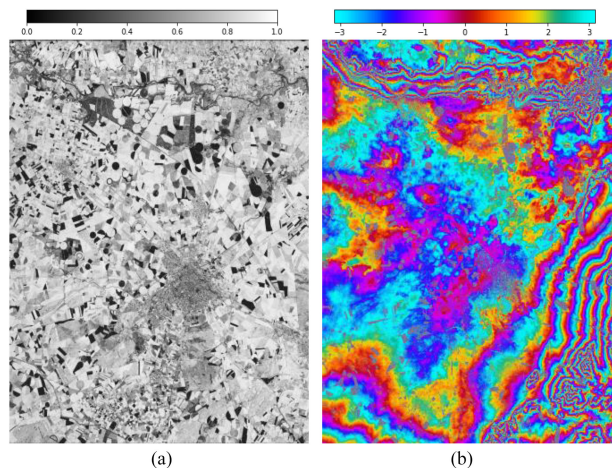

(a)   (b)

Fig. 14. (a) Coherence and (b) interferometric phase obtained between one TDX and one PAZ acquisition of the Albacete strip 13 dataset at HH polarization with 4 days temporal separation and 379 m perpendicular baseline. Coherence mean ($\pm \sigma$) values: 0.70 (± 0.22). (a) Coherence TDX 2019.11.25 and PAZ 2019.11.29. (b) Int. phase TDX 2019.11.25 and PAZ 2019.11.29.

atmospheric phase between repeat-pass TSX/TDX and PAZ will be similar to the observed between repeat-pass acquisition pairs of the same sensor under comparable atmospheric conditions. Section IV-C briefly analyzes the residual phase obtained over some interferograms, which may give an idea of the impact of this component.

B. Temporal Stability

In this section, the effect of the temporal separation on the coherence will be analyzed more in detail for the different test
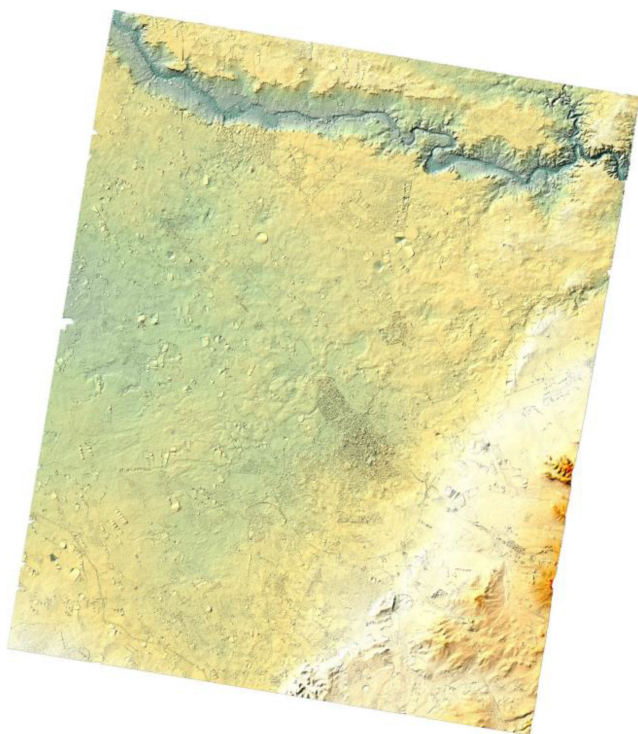
Fig. 15. 3-D representation (top view) of the geocoded DEM of Albacete generated from the interferogram between TDX and PAZ acquisitions of 2019.11.25 and 2019.11.29, respectively.

Fig. 16. Height difference between the singe-pass and repeat-pass DEMs generated over the Albacete test site and difference PDF. (a) Repeat-pass versus. single-pass DEM difference. (b) Repeat-pass versus single-pass DEM difference histogram.

sites and land cover types. For this analysis the Madrid strip 13 at HH polarization will be used, as it has the larger timespan within the TSX/TDX and PAZ acquisitions.

Fig. 17 shows the coherence obtained between PAZ and TDX pairs for different temporal separation from four days to two months. The land cover of the area may be seen on Fig. 18. The effect of the temporal decorrelation may be seen clearly on the forested areas on top of the image (in green color on Fig. 18), where the coherence is decreasing as the temporal separation between images increases. It is worth noticing that the coherence observed over forested areas in Fig. 17 is larger than the previously shown over the forest near Neustrelitz, where four days are enough to completely lose coherence. This may be caused due to the fact that the forest in Neustrelitz is much denser than in this area near Madrid. This example shows clearly how the different types of forest may have a different impact on the observed coherence due to different temporal decorrelation evolutions. It might also be seen that in the urban areas, appearing in red color in Fig. 18, the coherence is maintained even after two months temporal separation. This is caused by the presence of point scatters in man-made structures that are able to maintain long-term coherence.

The Albacete dataset may be used to get an idea of how the coherence is preserved over time on agricultural areas, as most of the scene is covered by agricultural fields. Figs. 14(a), 19(a), and 19(b) show the coherence obtained on Albacete between TDX and PAZ acquisitions for temporal separations of 4, 15, and 48 days, respectively. The perpendicular baselines between the images are quite similar: 379; 337; and 405 m, respectively.
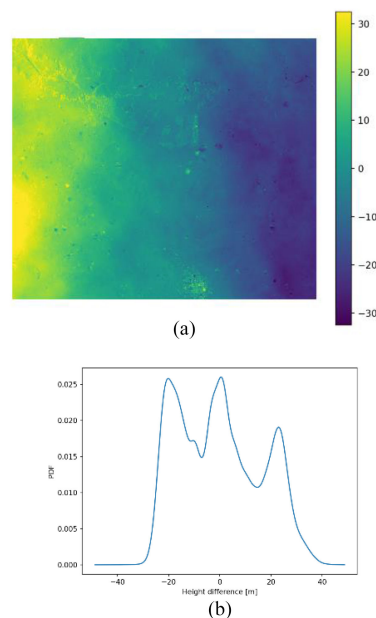
Fig. 20 shows the land cover distribution over the scene in the five simplified classes according to the CLC 2018 map.

It may be observed that, as the temporal separation increases, the coherence decreases due to temporal decorrelation. On the agricultural fields, however, there is also a binary behavior where some fields preserve the coherence over time while others appear in back. As described before, this is due to changes occurring on the agricultural fields, related to phenological changes or cultivation labor, resulting in a sudden drop of the coherence. As the temporal separation between acquisitions increases, the number of black fields due to changes also increases [19], [20].

The changes of coherence with respect to temporal separation may be seen in more detail in a 2-D joint PDF. Fig. 21 shows the joint distribution of the coherence with 4 days temporal separation [see Fig. 14(a)] versus the coherence with 15 and 48 days [see Fig. 19(a) and (b)] for each of the three main land cover types observed in Fig. 20: urban and industrial, agricultural and forested areas. The bare and water areas have not been considered as too few pixels are present on the scene in order to be representative. In these plots the horizontal axis corresponds to the coherence at the shorter temporal separation (4 days) while the vertical corresponds to the larger temporal difference, 15 days in Fig. 21(a), (c), and (e) plots and 48 days in Fig. 21(b), (d), and (f).

The decrease of coherence due to temporal decorrelation may be clearly seen in Fig. 21 as most of the distribution is below the white dashed line, corresponding to same coherence on both acquisition pairs. It is worth noticing that each of the different land cover types has a different temporal behavior, resulting in a different 2-D joint PDF. Therefore, the article of the temporal decorrelation might be a valuable input for land cover classification. This possibility has already been described
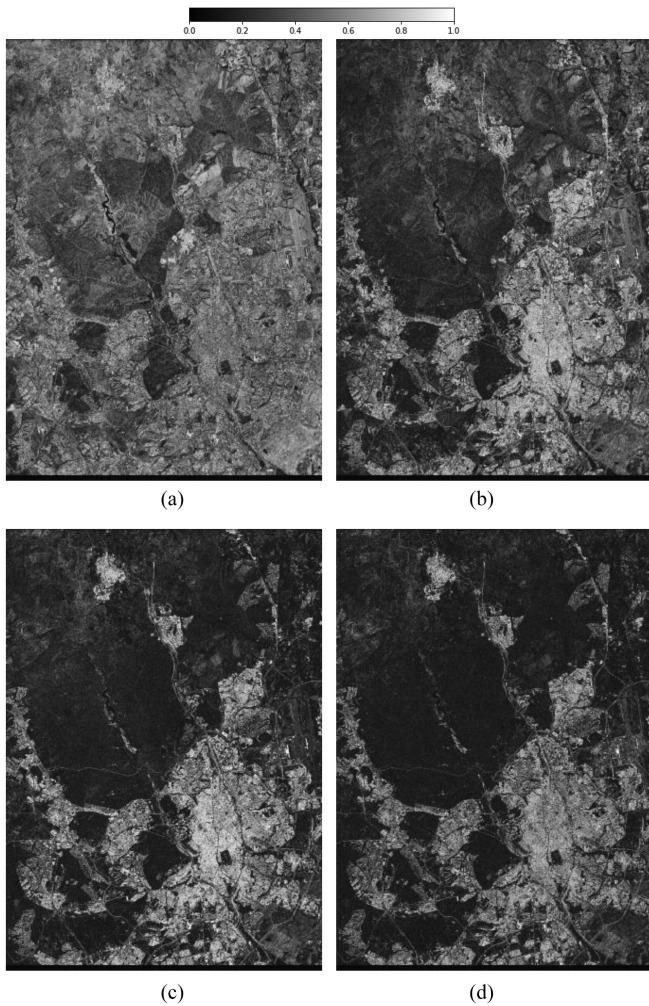
(a)   (b)

(c)   (d)

Fig. 17.   Coherence obtained between PAZ and TDX Madrid strip 13 acquisitions at HH polarization with (a) 4-day, (b) 18-day, (c) 51-day, and (e) 62-day temporal separation. Perpendicular baselines are (a) -85 m, (b) -2 m, (c) 8 m, and (d) 176 m. Coherence mean $(\pm\,\sigma)$ values: (a) 0.49 (± 0.22). (b) 0.42 (± 0.22). (c) 0.39 (± 0.22). (d) 0.36 (± 0.21). (a) Coherence PAZ 2020.01.28 and TSX 2020.01.24. (b) Coherence PAZ 2020.01.06 and TSX 2020.01.24. (c) Coherence PAZ 2019.12.04 and TSX 2020.01.24. (d) Coherence PAZ 2019.11.23 and TSX 2020.01.24.
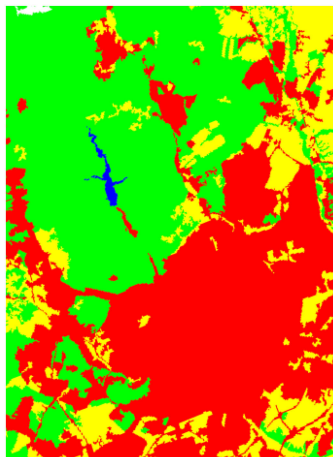

Fig. 18.   CLC 2018 land cover map of the Madrid strip 13 test site reduced to 5 classes.

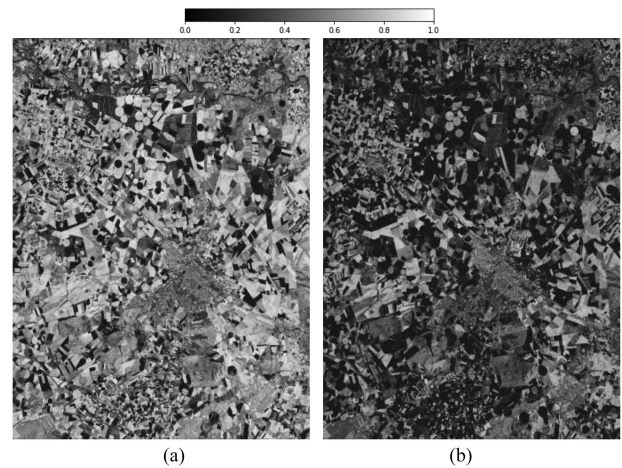
(a)   (b)

Fig. 19.   Coherence obtained between two TDX-PAZ acquisitions of the Albacete strip 13 dataset at HH polarization with (a) 15 days and (b) 48 days temporal separation and (a) 337 m and (b) 405 m perpendicular baseline. Coherence mean $(\pm\,\sigma)$ values. (a) 0.57 (± 0.24). (b) 0.41 (± 0.21). (a) Coherence TDX 2019.11.25 and PAZ 2019.12.10. (b) Coherence TDX 2019.11.25 and PAZ 2020.01.12.
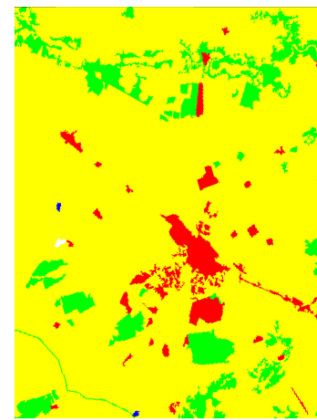

Fig. 20.   CLC 2018 land cover map of the Albacete strip 13 test site reduced to 5 classes.

in [14] and [20] and analyzed in [12]. As mentioned before, the decrease of coherence over forested areas, in Fig. 21(e) and (f), is clearly larger than in other land cover types. Over urban areas it may be clearly seen that some pixels preserve high values of coherence over time, corresponding to coherent scatters in man-made structures that are stable over time, appearing on the top right plot of Fig. 21(a) and (b). In Fig. 21(d), the binary behavior of agricultural fields, depending on if a change is observed or not, may be observed in the bimodal distribution appearing at the right part of the plot.

C. Residual Phase Analysis

For the assessment of the interferometric residual phase, the interferograms shown in Figs. 9(b), 9(d), and 14 will be employed. The flat earth and known topography components will be removed from each interferogram. For the removal of the topography, the DEM extracted from the corresponding
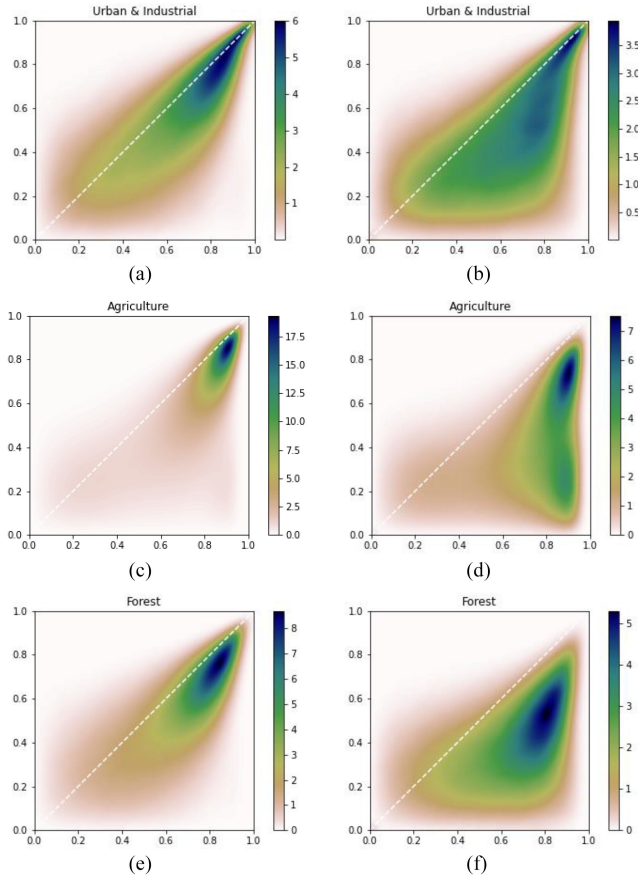
Fig. 21.   Joint PDF of coherences between different temporal separations on Albacete strip 13 dataset at HH polarization. Horizontal axis corresponds to a 4 days temporal difference while the vertical axis to 15 days and 48 days in the first and second column, respectively. Each row corresponds to a different type of land cover according to the simplified CLC 2018 map: urban; agriculture; and forest. (a) Urban 4–15 days. (b) Urban 4–48 days. (c) Agriculture 4–15 days. (d) Agriculture 4–48 days. (e) Forest 4–15 days. (f) Forest 4–48 days.

single-pass bistatic images acquired at the same polarization will be employed. The remaining phase after compensating for these components is shown in Fig. 22. It is worth mentioning that the residual phase may be composed by several factors as, for instance, atmospheric phase, orbital errors or subsidence between master and slave images. The image in Fig. 22(b) is smaller since the bistatic acquisition has a different coverage, as already mentioned in the previous section.

As it may be seen in Fig. 22(a), the residual phase over Madrid presents no significant fringes over the image. In some areas it may be slightly correlated with topography. This could be explained by atmospheric differences due to changes in pressure and temperature with height [31]. On the residual phase over Albacete in Fig. 22(b), however, some fringes may be observed in range direction. These fringes are producing the linear trend on the generated DEM, as shown in Fig. 16. In order to see if these changes may be caused by differences in the atmospheric conditions, meteorological data was consulted. No significant changes were observed between these days in terms of temperature or pressure, but a very light rain was detected on the master acquisition on 2019.11.25 which might be causing this effect due to changes in the atmospheric water vapor [29].
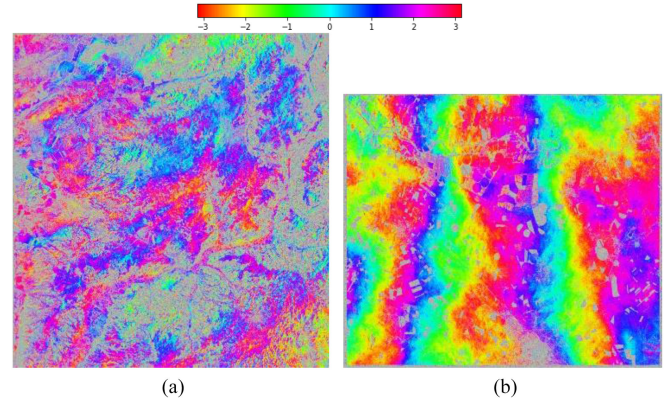

Fig. 22.   Residual phase obtained from Madrid and Albacete interferograms shown in Figs. 9(b), 9(d) and 14, respectively. The single-pass bistatic DEM has been used to remove topography. (a) Madrid PAZ 2019.12.09—TDX 2019.12.16. (b) Albacete TDX 2019.11.25—PAZ 2019.11.29.
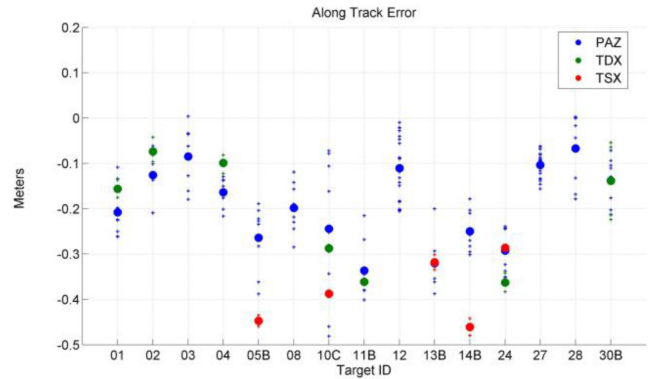

Fig. 23.   Along track CR location accuracy analysis.

D. Geolocation Accuracy

As a prerequisite for applications based on data fusion from the three systems, a geometric cross check has been carried out to verify that the pixel location accuracy in the complex images of PAZ is equivalent to the accuracy of TDX and TSX systems. Pixel location accuracy is a figure of merit with two main error sources: along and across track errors. Orbit precision determination accuracy aside, along track errors are dominated by the azimuth time shift caused by differences between radar and orbit times. Meanwhile, across track error will be mostly dominated by the accuracy in the calibration of the internal delay of each system. In order to correct the impact of the atmosphere on geolocation accuracy, ionosphere and tropospheric path delays have been considered, using the models included in PAZ processor, equivalent to the TerraSAR multimode SAR processor [28], [32].

In order to perform the geometric analysis, a subset of single look complex (SLC) images acquired with the three systems over the INTA calibration test site in Madrid are analyzed. The accuracy obtained for the three satellites in along and across track directions are compared in Figs. 23 and 24 and summarized in Tables VI and VII, respectively, where the root mean squared (RMS) error is shown for each satellite.
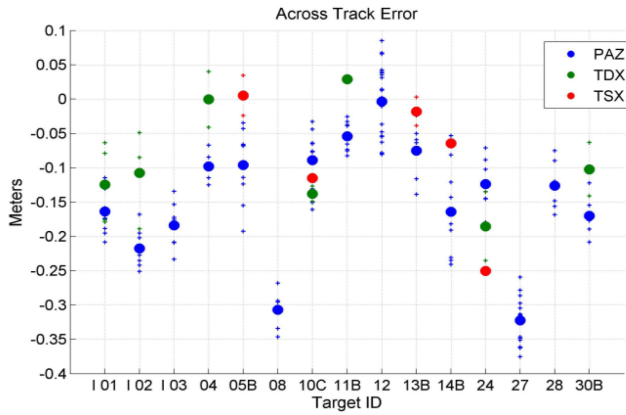
Fig. 24.   Across track CR location accuracy analysis.

Fig. 25.   Pixel location accuracy.

TABLE VI
RMS ALONG TRACK ERROR FOR EACH SYSTEM SAMPLES

Satellite	Along Track Error RMS (m)
TSX	0.401
TDX	0.313
PAZ	0.222

TABLE VII
RMS ACROSS TRACK ERROR FOR EACH SYSTEM SAMPLES

Satellite	Across Track Error RMS (m)
TSX	0.111
TDX	0.109
PAZ	0.186

TABLE VIII
PIXEL LOCATION ACCURACY: TSX-TDX-PAZ COMPARISON

Satellite	Pixel Location Accuracy RMS (m)
TSX	0.416
TDX	0.332
PAZ	0.290

Fig. 26.   Differences in northing and easting of CRs in Madrid.

It is worth noting that the PAZ system has an optimal RMS error value because the system has been calibrated with respect to this set of reflectors.

The calculated results are down to 20 cm for each mission, all of them in the order of scientific orbit determination performances, which indicates that the internal delay parameter has been well characterized.

Fig. 25 shows the total pixel location accuracy and Table VIII presents its RMS for each satellite. Analyzing the standard deviation of the pixel location accuracy for all cases, we could observe not only the high quality of the TSX, TDX, and PAZ satellite missions, but we can also conclude that the three systems

are quite similar in terms of geometric accuracy which would allow the users to work with them interchangeably.

Additionally, the geolocation accuracy was assessed with respect to a cartographic grid. For this purpose, the TSX and PAZ datasets were orthorectified using the TanDEM-X DEM and transformed into the Universal Transverse Mercator projection. The positions of the CRs in Madrid and Neustrelitz were measured in the TSX and PAZ image data and compared to their positions determined by GPS.

The position differences of 10 CRs deployed at the Madrid site (see Fig. 26) and another four of the Neustrelitz calibration field (see Fig. 27) were analyzed.

The maximum deviation was 13.50 m, the minimum 0.03 m, both at the Madrid site. The maximum appeared in the easting direction, which is sensitive to a height error induced pixel displacement. In this case, the height of the CR and the one from the TanDEM-X DEM differ by a few meters. The overall location accuracy of all CRs as provided in Table IX is comparable for PAZ and TSX.

Analyzing the standard deviation of the pixel location accuracy and the RMS of the geopositioning for all cases, we could observe not only the high quality of the TSX, TDX, and PAZ sa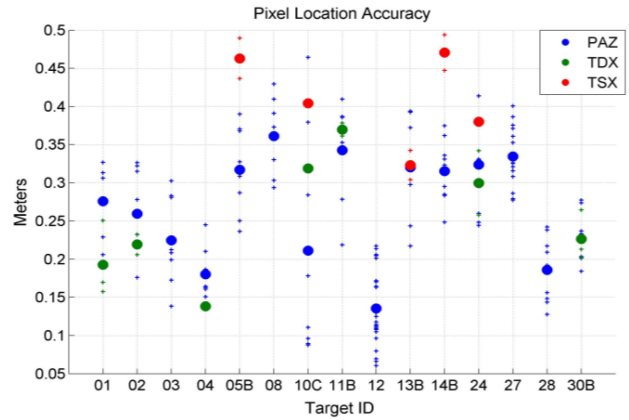tel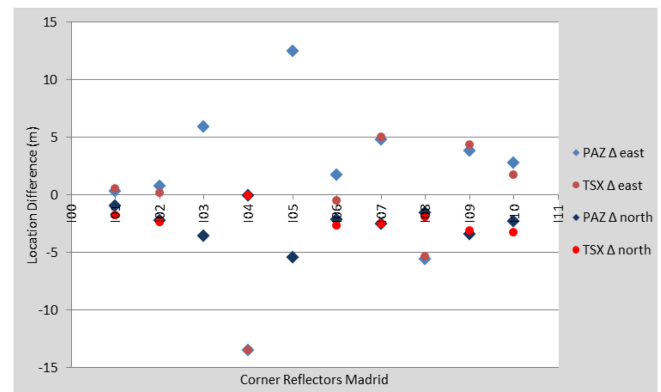lite missions, but we can conclude that the three systems are quite similar in terms of geometry accuracy which would allow the users to work with them interchangeably.
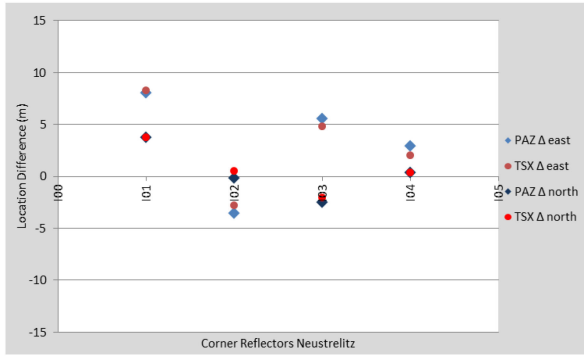
Fig. 27.   Differences in northing and easting of CRs in Neustrelitz.

TABLE IX
LOCATION ACCURACY IN NORTHING AND EASTING

Satellite	RMS easting (m)	RMS northing (m)
PAZ	6.38	2.67
TSX	5.49	2.33

V. DATA PERFORMANCE

All the previous experiments have demonstrated the good quality obtained by the TanDEM-X and PAZ pairs. On the one hand, the geolocation accuracy is very similar for both missions which makes possible the combination of both missions for increased revisit time. On the other hand, the interferograms obtained between both sensors present good coherences and no degradation is observed in comparison with interferometric pairs between acquisitions of the same sensor.

Moreover, the possibility to obtain interferograms with a temporal difference of just 4 and 7 days instead of 11 days reduces the temporal decorrelation improving the coherence. In this regard, it has been shown that temporal decorrelation over the dense forest near Neustrelitz is the main limitation at X-band, and even four days may be enough to completely decorrelate the signal. However, over the not so dense forest near Madrid test site the decorrelation is not so strong. Over agricultural areas the coherence obtained by these pairs is generally higher. However, a dual behavior has been observed. The fields that do not present a change appear with high coherence while those that change between the acquisitions exhibit a significant drop in the coherence. It is worth noticing that the number of changing fields increases with the temporal distance between pairs, reducing the overall coherence on the scene. Here it is worth mentioning that the analysis was performed in winter, and a different agricultural field dynamic may be observed in summer, for instance. Finally, over urban areas some pixels may preserve high coherence over time, corresponding to stable man-made structures.

To illustrate the quality of the obtained interferometric TanDEM-X and PAZ four days interferometric pairs, some DEMs have been generated over Madrid and Albacete test sites. The quality obtained is generally good and has been compared with single-pass bistatic acquisitions. The effect of temporal decorrelation and residual phase due to repeat-pass acquisitions over the obtained DEMs has been briefly analyzed. While

temporal decorrelation may lead to phase unwrapping errors resulting into errors at small scales, residual phase components like atmospheric phase may lead to large scale variations. These variations, however, are inherent to any repeat-pass acquisition and are not related to the interoperability between sensors.

VI. DATA AVAILABILITY AND PERSPECTIVE

The good data performance makes it possible to open selected test sites for the science community. The TSX/TDX -PAZ constellation with an optimized revisit time and increased acquisition capacity will be available to the science community in the frame of joint announcement of opportunity call. The call will include the definition of specific reference super test sites, specifically selected to cover a wide range of application areas, such as agriculture, forestry, volcanology, sea ice, glaciers and others.

Interested users will be kindly asked to submit their proposals to DLR [22] and INTA [23] for the independent revision and approval of each institution with the request to have joint data acquisitions.

Different acquisition scenarios can be considered by the users as follows.

1) Acquisition of pursuit monostatic datasets (combination of PAZ and one out of TerraSAR-X or TanDEM-X), which can be utilized for, e.g., repeat pass interferometry; (repeat pass of 4–7 days).
2) Combination of all three satellites will allow the derivation of two pursuit monostatic pairs (PAZ-TerraSAR-X, PAZ-TanDEM-X)
3) One bistatic image pair (TerraSAR-X-TanDEM-X) for advanced studies. The latter will e.g., allow interferometry studies of temporal decorrelation for natural targets, or allow the derivation of change detection products, or pseudoquad-pol datasets.

This article could prove that the performance of the joint experiments is of high quality when combining TSX/TDX with PAZ to retrieve coregistered SLC data with a higher repeat time than acquiring them independently. The datasets acquired over the selected sites are unique and will open up new opportunities for the development of a wide range of applications.

REFERENCES

[1] G. Krieger et al., "TanDEM-X: A satellite formation for high-resolution SAR interferometry," IEEE Trans. Geosci. Remote Sens., vol. 11, no. 45, pp. 3317–3341, Nov. 2007.

[2] M. Zink et al., "TanDEM-X: The new global DEM takes shape," IEEE Geosci. Remote Sens. Mag., vol. 2, no. 2, pp. 8–23, Jun. 2014, doi: 10.1109/MGRS.2014.2318895.

[3] R. Werninghaus and S. Buckreuss, "The TerraSAR-X mission and system design," IEEE Trans. Geosci. Remote Sens., vol. 48, no. 2, pp. 606–614, Feb. 2010.

[4] W. Pitz and D. Miller, "The TerraSAR-X satellite," IEEE Trans. Geosci. Remote Sens., vol. 48, no. 2, pp. 615–622, Feb. 2010.

[5] R. Bamler and P. Hartl, "Synthetic aperture radar interferometry," Inverse Problem, vol. 14, no. 4, pp. R1–R54, 1998.

[6] A. Bojarski et al., "TanDEM-X long-term system performance after 10 years of operation," IEEE J. Sel. Topics Appl. Earth Observ. Remote Sens., vol. 14, pp. 2522–2534, Jan. 2021, doi: 10.1109/JSTARS.2021.3055546.

[7] A. Bojarski et al., "A decade of TerraSAR-X and TanDEM-X operation: A retrospective on the performance of the SAR system and an outlook to the future," in Proc. CEOS SAR Workshop, 2019, pp. 1–20. [Online]. Available: https://earth.esa.int/documents/700255/4038563/6+Bojarsky.pdf

[8] T. Fritz, J. Mittermayer, B. Schättler, W. Balzer, S. Buckreuß, and R. Werninghaus, "TerraSAR-X ground segment, level 1b product format specification (no. TX-GS-DD-3307)," in *Proc. Cluster Appl. Remote Sens.*, 2007, pp. 1–257.

[9] European Environment Agency (EEA) Copernicus Land Monitoring Service, Chicago, IL, USA, Corine Land Cover (CLC) 2018, Version 2020_20u1.[Online]. Available: https://land.copernicus.eu/pan-european/corine-land-cover/clc2018

[10] H. A. Zebker and J. Villasenor, "Decorrelation in interferometric radar echoes," *IEEE Trans. Geosci. Remote Sens.*, vol. 30, no. 5, pp. 950–959, Sep. 1992.

[11] S. Cloude, *Polarisation: Applications in Remote Sensing*. Oxford, U.K: Oxford Univ. Press, 2009.

[12] F. Sica *et al.*, "InSAR decorrelation at X-Band from the joint TanDEM-X/PAZ constellation," *IEEE Geosci. Remote Sens. Lett.*, to be published, doi: 10.1109/LGRS.2020.3014809.

[13] J. I. Askne, P. B. Dammert, L. M. Ulander, and G. Smith, "C-band repeat-pass interferometric SAR observations of the forest," *IEEE Trans. Geosci. Remote Sens.*, vol. 35, no. 1, pp. 25–35, Jan. 1997.

[14] L. Bruzzone, M. Marconcini, U. Wegmuller, and A. Wiesmann, "An advanced system for the automatic classification of multitemporal SAR images," *IEEE Trans. Geosci. Remote Sens.*, vol. 42, no. 6, pp. 1321–1334, Jun. 2004.

[15] M. Martone, B. Bräutigam, P. Rizzoli, C. Gonzalez, M. Bachmann, and G. Krieger, "Coherence evaluation of TanDEM-X interferometric data," *ISPRS J. Photogramm. Remote Sens.*, vol. 73, pp. 21–29, 2012.

[16] G. Krieger *et al.*, "TanDEM-X: A radar interferometer with two formation-flying satellites," *Acta Astronautica*, vol. 89, pp. 83–98, 2013.

[17] P. Prats *et al.*, "TAXI: A versatile processing chain for experimental TanDEM-X product evaluation," in *Proc. IEEE Int. Geosci. Remote Sens. Symp.*, Jul. 2010, pp. 4059–4062.

[18] M. Martone *et al.*, "The global forest/non-forest map from TanDEM-X interferometric SAR data," *Remote Sens. Environ.*, vol. 205, pp. 352–373, 2018.

[19] J. Kemp and J. Burns, "Agricultural monitoring using pursuit monostatic TanDEM-X coherence in the Western Cape, South Africa," in *Proc. 11th Eur. Conf. Synthetic Aperture Radar*, Jun. 2016, pp. 1–4.

[20] M. Busquier, J. M. Lopez-Sanchez, A. Mestre-Quereda, E. Navarro, M. P. González-Dugo, and L. Mateos, "Exploring TanDEM-X interferometric products for crop-type mapping," *Remote Sens.*, vol. 12, no. 11, pp. 1–4, 2020.

[21] TanDEM-X Payload Ground Segment CoSSC Generation and Interferometric Considerations, TD-PGS-TN-3129, 2012.

[22] TanDEM-X Science Server to submit data acquisition proposals. [Online]. Available: https://tandemx-science.dlr.de/

[23] PAZ Ciencia, *PAZ Sci. Activities, web interface for Sci. user community PAZ*: [Online]. Available: https://www.inta.es/paz-ciencia/en/

[24] A. S. González, M. Labriola, J. C. Soteras, and J. S. Palma, "PAZ instrument design and performance," in *Proc. 3rd Int. Asia-Pac. Conf. Synthetic Aperture Radar*, Sep. 2011, pp. 1–4.

[25] M. J. González, E. Vega, N. Alfaro, and B. Gómez, "PAZ ground segment," in *Proc. IEEE Int. Geosci. Remote Sens. Symp.*, 2012, pp. 4579–4581.

[26] M. J. G. Bonilla, J. M. C. Munoz, and M. G Rodriguez, "PAZ product definition procedure," in *Proc. 12th Eur. Conf. Synthetic Aperture Radar*, 2018, pp. 1–4.

[27] N. C. Vazquez, P. C. Revenga, N. G. Martinez, A. L. Pescador, J. M. C. Munoz, and J. R Larranaga-Sudupe, "INTA calibration field deployment and management. First experiences after PAZ launch," in *Proc. 12th Eur. Conf. Synthetic Aperture Radar*, 2018, pp. 1–4.

[28] H. Breit, T. Fritz, U. Balss, M. Lachaise, A. Niedermeier, and M. Vonavka, "TerraSAR-X SAR processing and products," *IEEE Int. Geosci. Remote Sens.*, vol. 48, no. 2, pp. 727–740, Feb. 2010.

[29] H. A. Zebker, P. A. Rosen, and S. Hensley, "Atmospheric effects in interferometric synthetic aperture radar surface deformation and topographic maps," *J. Geophys, Res., Solid Earth*, vol. 102, no. B4, pp. 7547–7563, 1997.

[30] P. Milillo, B. Riel, B. Minchew, S. H. Yun, M. Simons, and P. Lundgren, "On the synergistic use of SAR constellations' data exploitation for earth science and natural hazard response," *IEEE J. Sel. Topics Appl. Earth Observ. Remote Sens.*, vol. 9, no. 3, pp. 1095–1100, Mar. 2016.

[31] R. Iglesias *et al.*, "Atmospheric phase screen compensation in ground-based SAR with a multiple-regression model over mountainous regions," *IEEE Trans. Geosci. remote Sens.*, vol. 52, no. 5, pp. 2436–2449, May 2014.

[32] M. J. González, J. M. Cuerda, and M. García, "PAZ product definition procedure," in *Proc. 12th Eur. Conf. Synthetic Aperture Radar*, 2018, pp. 1–4.

Alberto Alonso-Gonzalez (Member, IEEE) received the B.Sc. degree in computer science, the M.Sc. degree in telecommunication engineering, and the Ph.D. degree from the Technical University of Catalonia, Barcelona, Spain, in 2007, 2009, and 2014, respectively.

Between 2009 and 2014, he was with the Department of Signal Theory and Communications, Technical University of Catalonia. Since June 2014, he has been with the Microwaves and Radar Institute, German Aerospace Center, Wessling, Germany, as a Member of the Polarimetric SAR Interferometry research group. His research interests include multidimensional synthetic aperture radar (SAR), SAR polarimetry and interferometry, digital signal and image processing.

His current research activities are focused on SAR data modeling and decomposition techniques for the retrieval of biophysical information for agricultural and forest monitoring.

Dr. Alonso-Gonzalez was the recipient of the First Place Student Paper Award at the EUSAR 2012 Conference and the Extraordinary Doctoral Thesis Award, by the Technical University of Catalonia, in 2016.

Nuria Gimeno Martínez received the M.Sc. degree of Telecommunication Engineering from de University of Alcalá, Madrid, Spain, in 2007.

In 2008, she joined INTA, the Spanish National Institute for Aerospace Technology, Spain, as an External Consultor with the Radar Laboratory, being responsible of the development of the Real Time SAR data processor subsystems of airborne platforms of the Radar Laboratory. She participated in the implementation of SAR signal processing algorithms. Since 2012, she has been a Member of PAZ calibration/validation Team, working in the development of tools for the calibration and exploitation of polarimetric products from the PAZ satellite. Her research interests include in the implementation of calibration, instrument operation processes, polarimetric tools and in the validation of interferometric PAZ data.

Irena Hajnsek (Fellow, IEEE) received the Dipl. Degree (Hons.) in fluvial river systems from the Free University of Berlin, Berlin, Germany, in 1996, and the Dr. rer. nat. degree (Hons.) in model-based estimation of soil moisture from fully polarimetric Synthetic Aperture Radar, Friedrich Schiller University of Jena, Jena, Germany, in 2001.

Since November 2009, she has been a Professor of earth observation with the Institute of Environmental Engineering, Swiss Federal Institute of Technology (ETH), Zürich, Switzerland, and the Head of the Polarimetric SAR Interferometry research Group, the German Aerospace Center Microwaves and Radar Institute. Since 2010, she has been the Science Coordinator of the German satellite mission TanDEM-X and proposed satellite mission Tandem-L. Her main research interests are in electromagnetic propagation and scattering theory, radar polarimetry, SAR and interferometric SAR data processing techniques, environmental parameter modelling and estimation.

Dr. Hajnsek was a Technical Program Co-chair of the IEEE IGARSS 2012 in Munich, Germany, and 2019 in Yokohama, Japan. Since 2013, she has been a Member of the IEEE GRSS AdCom and from 2016 to 2020, she was the Vice President of the IEEE GRSS Technical Committees.

Patricia Cifuentes Revenga received the Diploma degree in topography engineering from University of Oviedo, Asturias, Spain, in 2005 and the M.Sc. degree in cartography and geodesy engineering from the University of Alcalá, Madrid, Spain, 2008.

In 2008, she was with ISDEFE, working with the Radar Laboratory, National Institute of Aerospace Technology (INTA) developing a geocoding software for SAR interferograms. In 2012, she joined the INTA calibration and validation team for PAZ Mission. She currently works particularly developing an external calibration tool for SAR products.

Ursula Marschalk received the Graduate engineer (Dipl.-Ing. FH) degree in cartography from the University of Applied Sciences Munich, Munich, Germany, in 1991.

In 1990, she with the German Aerospace Centre (DLR) at the Division for Planetary Research as the Head of the Regional Planetary Image Facility. In 1991, she was with the DLR's German Remote Sensing Data Center, where she was involved in the implementation and operation of a SAR geocoding system for the ERS- and X-SAR-missions. Since 1996, he has been focussing on the generation of Digital Elevation Models from SAR data for several missions (ERS-1/2, SRTM/X-SAR, TanDEM-X).

María José González Bonilla was born in Madrid, Spain. She received the M.S degree in telecommunication engineering from the Universidad de Alcalá, Madrid, Spain, in 2006.

Since 2002, she has been with the Spanish National Institute of Aerospace Technology, where she gained experience in SAR processing and calibration. In 2008, she was engaged in the Spanish PAZ mission (SAR satellite), where she was responsible for the Payload Data Ground Segment development. She is currently the CEIT Operations Manager and a PAZ Science Activities Coordinator.

Nuria Casal Vázquez received the B.Sc. degree in surveying engineering, in 2004, and the M.Sc. degree in geodesy and cartography engineering from the Universidad Politécnica de Madrid, Madrid, Spain, in 2006.

Since 2004, she has been with the National Institute of Aerospace Technology (INTA) developing SAR airborne geocoding processor and designing SAR mission campaigns. She currently works on calibration- validation and Scientific Exploitation within the PAZ mission.

Christo Grigorov received the M.Sc. degree in computer science from the Technical University Sofia, Sofia, Bulgaria, in 2005 and the double M.Sc. degree in space science and technology from the Julius-Maximilians University of Wuerzburg, Wuerzburg, Germany, and from the Lulea University of Technology, Luleå, Sweden, in 2007. In 2008, he was with the Microwaves and Radar Institute (HR), German Aerospace Center (DLR), Germany. He has been working as a Systems Engineer and a Software Engineer for ground segments of radar satellite missions, such as TerraSAR-X and TanDEM-X with focus on system design, integration and implementation of new features. He leads the Systems Engineering team with DLR HR. Since 2009, he has been a Member of the International Council on Systems Engineering and a holder of the INCOSE Associate Systems Engineering Professional certificate.

Juan Manuel Cuerda born in Albacete, Spain. He received the M.S. degree in telecommunication engineering from Universidad Politécnica de Madrid, Madrid, Spain.

In 2003, he was with the National Institute of Aerospace Technology, where he worked on real time SAR image formation algorithms for airborne prototypes. In 2010, he joined PAZ Mission team and, since 2015, coordinates the PAZ Calibration and Validation Team activities, including PAZ commissioning phase and routine calibration and system monitoring campaigns. He is currently the SAR Space Systems and Calibration Manager.

Achim Roth received the Graduate engineer (Dipl.-Ing.) degree in geodesy from the University of Karlsruhe, Karlsruhe, Germany, in 1987.

In 1987, he was with the German Aerospace Centre for the development and implementation of an operational SAR-geocoding system for the ERS- and X-SAR-missions. Since 1991, he has been leading the team "SAR Topography" with DLR's German Remote Sensing Data Center. From 2000 to 2004, he was the SRTM/X-SAR Ground Segment Manager. Since 2002, he has been the TerraSAR-X Science Coordinator. It contributed to the Shuttle Radar Topography Mission (SRTM) and is currently involved in the TerraSAR-X and TanDEM-X missions. His research interests include the development of geoinformation products from SAR data, the corresponding retrieval techniques and their implementation as operational processors.

Marcos García Rodríguez received the M.Sc. degree in computer engineering from the Universidad Politecnica de Madrid, Madrid, Spain in 1994.

Since 1992, he has been with the Spanish National Institute of Aerospace Technology (INTA), where he was working in the development of the airborne SAR systems of the Institute. Since 2008, he has been involved in the development of the PAZ Ground Segment and contributed in the PAZ satellite development as Technical Assistant. He is a Member of the INTA's SAR calibration team, working in the PAZ calibration activities in commissioning and operational phases. He is currently the Head of the RADAR Technology Group, INTA.